

**Simultaneous energy harvesting and storage via solar-driven regenerative electrochemical cycles**

Journal:	<i>Energy &amp; Environmental Science</i>
Manuscript ID	EE-ART-06-2019-001930.R1
Article Type:	Paper
Date Submitted by the Author:	20-Sep-2019
Complete List of Authors:	Ding, Yu; The University of Texas at Austin, Materials Science and Engineering Guo, Xuelin; The University of Texas at Austin, Materials Science and Engineering Ramirez-Meyers, Katrina; The University of Texas at Austin, Materials Science and Engineering Zhou, Yangen; The University of Texas at Austin, Materials Science and Engineering Zhang, Leyuan; The University of Texas at Austin, Materials Science and Engineering Zhao, Fei; The University of Texas at Austin, Materials Science and Engineering Yu, Guihua; The University of Texas at Austin, Materials Science and Engineering

## PAPER

## Simultaneous energy harvesting and storage via solar-driven regenerative electrochemical cycles†

Cite this: DOI: 10.1039/x0xx00000x

Yu Ding,<sup>a§</sup> Xuelin Guo,<sup>a§</sup> Katrina Ramirez-Meyers,<sup>a</sup> Yangen Zhou,<sup>a</sup> Leyuan Zhang,<sup>a</sup> Fei Zhao<sup>a</sup> and Guihua Yu<sup>\*a</sup>Received 00th January 2019,  
Accepted 00th February 2019

DOI: 10.1039/x0xx00000x

[www.rsc.org/ees](http://www.rsc.org/ees)

Solar energy is regarded as the most promising source of electricity considering its large magnitude on earth every day. The effective use of such an intermittent energy source relies on development of affordable, inexhaustible and clean solar energy conversion and storage technologies. Here, we design a novel solar-driven regenerative electrochemical system for simultaneous photoelectric energy harvesting and storage. With rational screening of redox species and comprehensive electrochemical study, a high Seebeck coefficient of  $-1.8 \text{ mV K}^{-1}$  is achieved by solely exploiting earth-abundant materials based on thermogalvanic effect. The high energy conversion efficiency (1.23%, and 11.9% versus Carnot efficiency) is achieved under a low temperature gradient of  $35 \text{ }^\circ\text{C}$ . Moreover, the durability of the proof-of-concept device has been examined under solar irradiation employing the bifunctional current collector/solar absorber with good electrical conductivity, efficient solar absorption and photothermal transduction. This innovative cell design integrating simultaneous energy conversion and storage represents an alternative approach towards cost-effective harnessing of solar energy and even more broad thermal energy in the ambient environments.

## Introduction

Solar energy as a renewable source of energy, is the most important energy source for all life forms in the world.<sup>1</sup> The vast amounts of solar energy available on earth make it a highly appealing source of electricity for human beings. Since the first solar cell built in the 1880s, a range of

### Broader context

Developing cost-effective devices based on earth-abundant materials for large-scale solar energy conversion and storage is crucial to alleviate the potential energy crisis in modern society. Here we report a novel electrochemical system for simultaneous energy harvesting and storage based on the thermogalvanic effect of rationally selected redox species. A regenerative electrochemical cell is demonstrated, employing the bifunctional current collector/solar absorber fabricated by a scalable process, for simultaneous energy harvesting and storage under solar irradiation without optical concentrators or accessory batteries. This neoteric device provides a roadmap for the development of innovative systems to harvest and store the solar energy and more broad thermal energy by using inexpensive, simple and stable materials.

ever-evolving technologies have been developed for efficient utilization of solar energy.<sup>2-5</sup> Currently the solar power generation is dominated by photovoltaic systems harnessing solar energy directly and concentrated solar power plants based on solar thermal energy.<sup>6-7</sup> Given the intermittent nature of solar energy, simultaneous conversion and storage of the electricity generated is important to deliver dispatchable power on demand, especially in remote sites.<sup>8</sup>

Here we report a novel cost-effective solar-driven regenerative electrochemical system for simultaneous photoelectric energy harvesting and delivery based on the principle of thermogalvanic effect.<sup>9-10</sup> Thermogalvanic cells represent a promising type of heat-empowered devices, but the energy conversion efficiency, ranging from 0.004% to 0.2%, is far less competitive than other power generation systems, limiting the applications for solar energy utilization.<sup>9,11</sup> Distinguished from conventional nonisothermal thermoelectric generators and thermogalvanic cells, here we build an isothermal heat engine-based electrochemical cell by rational selection of two redox species with similar redox potentials but opposite Seebeck coefficients. The

<sup>a</sup> Materials Science and Engineering Program and Department of Mechanical Engineering, The University of Texas at Austin, Austin, Texas 78712, USA. Email: [ghyu@austin.utexas.edu](mailto:ghyu@austin.utexas.edu)

<sup>§</sup> These authors contributed equally to this work

<sup>†</sup> Electronic Supplementary Information (ESI) available. See DOI: 10.1039/c000000x/

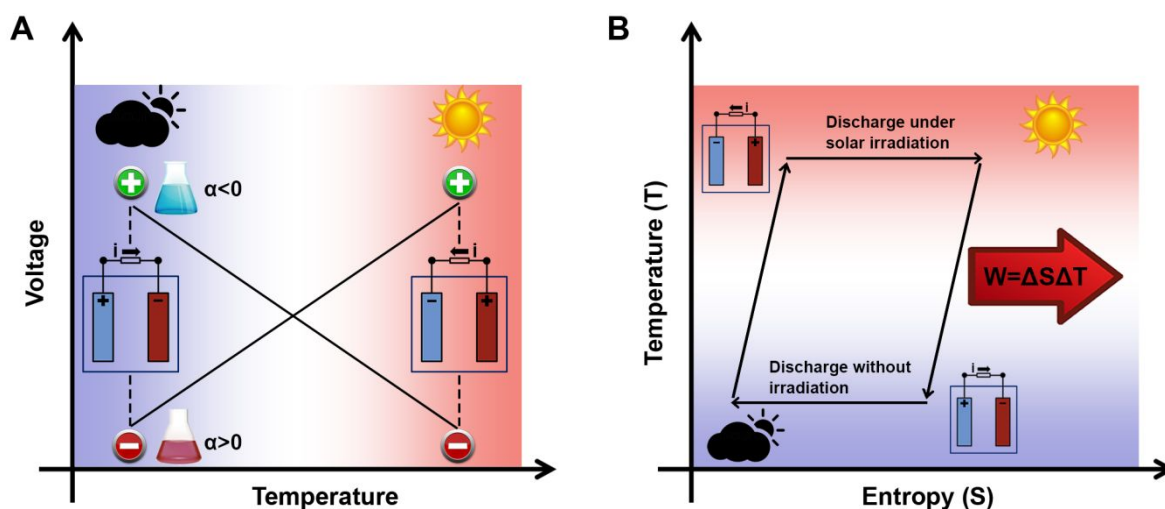


**Fig. 1** The working principle and cell design for the solar-driven regenerative electrochemical system. (A) Schematic showing the criteria to design the electrochemical cell for simultaneous energy harvesting and delivery. At room temperature, the cathode redox species with a higher potential possesses a negative Seebeck coefficient ( $\alpha$ ), and the anode redox species with a lower potential possesses a positive  $\alpha$ . Meanwhile, the potential shift of the full cell due to the temperature change under solar irradiation need be large enough to offset the potential difference between the cathode and anode redox species at room temperature. (B) Temperature-entropy diagram of the solar-driven regenerative electrochemical cycle, in which the energy output in one cycle is the area of the loop ( $\Delta S\Delta T$ ).

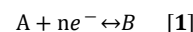
designated positive and negative electroactive species at high temperature are the negative and positive electroactive species at low temperature, respectively (Fig. 1A). The direction of current flow generated by thermal energy is reversed without any assistive electricity. The working principle of such a solar-driven regenerative electrochemical cell is analogous to a seesaw, in which two objects with similar weights sit on the two ends, and the seesaw rocks back and forth forever as long as a torque difference can be maintained alternately all the time. Likewise, temperature functions as the driving force to keep the alternate potential difference of the solar-driven regenerative electrochemical cell, thus leading to the simultaneous energy harvesting, storage, and delivery, and the energy output in one electrochemical cycle is the area of the loop in Fig. 1B.

Moreover, by localizing the solar thermal energy on the current collector where the redox reaction takes place instead of heating the bulk electrolyte solution, the heat loss can be minimized, thus contributing to the enhanced energy conversion efficiency. Meanwhile, the graphene-modified current collector, with high electrical conductivity, good light absorption and photothermal transduction, works as a solar absorber simultaneously, which not only facilitates the reaction kinetics but also enables broadband and efficient solar absorption. This neoteric energy system is solely based on cost-effective electrode materials without stringent manufacturing processes or costly solar concentrators.<sup>12</sup> Via rational design of both the redox species and the bifunctional current collector/solar absorber, an innovative solar-driven regenerative electrochemical system is demonstrated for integrated energy harvesting and storage under solar irradiation without concentrators or auxiliary batteries.

## Results and discussion

As illustrated in Fig. 1, the Seebeck coefficients of the two redox species in our proposed design should be opposite and of high magnitude

to maximize output voltage. A series of redox molecules are studied for rational screening of electroactive molecules. For a given electrochemical reaction of the form:



the relationship between Gibbs free energy change,  $\Delta G$ , and redox potential,  $E$ , is defined as

$$\Delta G = -nEF \quad [2]$$

where  $n$  is the number of electrons transferred in this reaction, and  $F$  is the Faraday constant. Meanwhile, the differential form of Gibbs free energy ( $dG$ ) is related to two natural variables: temperature ( $T$ ) and pressure ( $P$ ),

$$dG = -SdT + VdP \quad [3]$$

where  $S$  is the entropy, and  $V$  is the volume. Therefore, the Seebeck coefficient,  $\alpha$ , of the electrochemical reaction at constant pressure equals:

$$\alpha = \frac{\partial E}{\partial T} = -\frac{1}{nF} \frac{\partial \Delta G}{\partial T} = \frac{\Delta S}{nF} = \frac{(S_B + S_B^*) - (S_A + S_A^*) - nS_e}{nF} \quad [4]$$

where  $S_B$  and  $S_A$  are the partial molar entropies of products  $B$  and reactants  $A$ , respectively;  $S_B^*$  and  $S_A^*$  are the Eastman entropies of the transport of the respective ions that accompanies heat transfer;  $S_e$  is the transported entropy of electrons in metallic electrodes.<sup>13</sup> In most cases,  $S_e$  contributes only 1% of the total entropies, and the Eastman entropy caused by the Soret effect is negligible in a short timescale. Therefore, the Seebeck coefficient equation can be simplified to:

$$\alpha = \frac{S_B - S_A}{nF} \quad [5]$$

where  $\alpha$  solely depends on the entropy change in the redox reaction. Similar to a Carnot heat engine, in which the thermal energy available

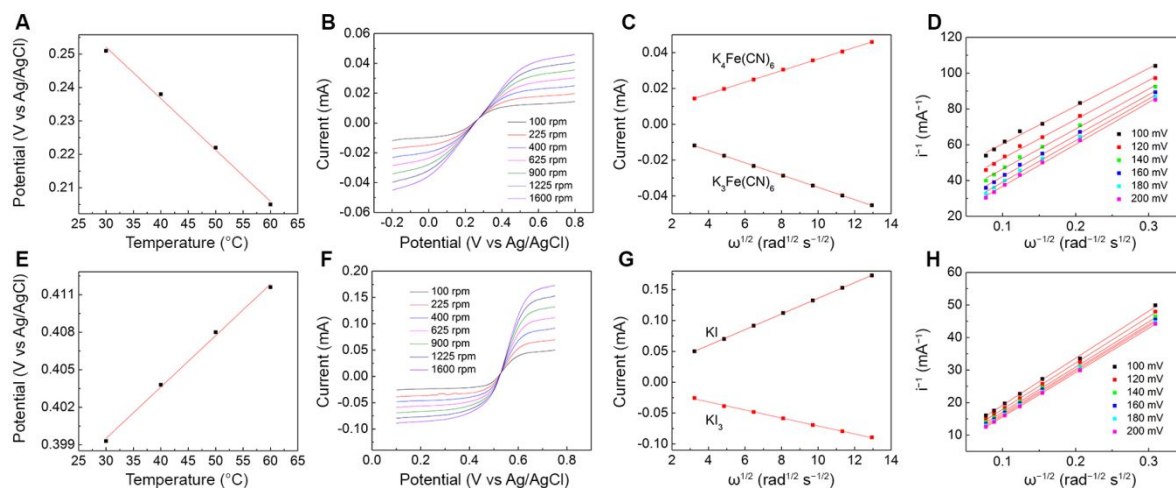


**Fig. 2** Seebeck coefficient measurements and RDE test of the selected redox species. (A–D) The Seebeck coefficient measurement, RDE test at a scan rate of  $10 \text{ mV s}^{-1}$ , Levich plot, and Koutecky–Levich plot derived from different overpotentials of  $\text{K}_3\text{Fe}(\text{CN})_6/\text{K}_4\text{Fe}(\text{CN})_6$  solution, respectively. (E–H) The Seebeck coefficient measurement, RDE test at a scan rate of  $10 \text{ mV s}^{-1}$ , Levich plot, and Koutecky–Levich plot derived from different overpotentials of  $\text{KI}_3/\text{KI}$  solution, respectively.

for harvest is proportional to the entropy change and temperature difference, a large entropy change is preferred in the regenerative electrochemical system. Thermodynamically, entropy indicates the amount of disorder in a system and  $\Delta S$  dictates the voltage delivered by the cell. Fig. 2A and 2E, and Fig. S1–S3 (ESI†) show the dependence of open circuit voltage on temperature of various types of redox species, including inorganic, organic, and organometallic molecules, namely,  $\text{K}_3\text{Fe}(\text{CN})_6/\text{K}_4\text{Fe}(\text{CN})_6$ ,  $\text{KI}_3/\text{KI}$ ,  $\text{CuSO}_4/\text{Cu}$ , 1,4-benzoquinone(BQ)/hydroquinone ( $\text{H}_2\text{BQ}$ ), 4-OH-2,2,6,6-tetramethyl-1-piperidinyloxy<sup>+</sup> (4-OH-TEMPO<sup>+</sup>)/4-OH-TEMPO, and (ferrocenylmethyl)trimethylammonium<sup>+</sup> chloride ( $\text{FcN}^+\text{Cl}$ )/ $\text{FcNCl}$ . The calculated Seebeck coefficients, summarized in Table S1 (ESI†), are typically smaller for organic and organometallic molecules compared to inorganic alternatives. The TEMPO and ferrocene derivatives show especially low  $\alpha$ -values, possibly due to the negligible variation of the molecular structures during the electron transfer processes.<sup>14</sup> Given the design criteria illustrated in Fig. 1,  $\text{K}_3\text{Fe}(\text{CN})_6/\text{K}_4\text{Fe}(\text{CN})_6$  and  $\text{KI}_3/\text{KI}$  are selected as the electroactive species for the solar-driven regenerative electrochemical cell due to their similar redox potentials and competitive Seebeck coefficients. Despite a larger  $\alpha$  of  $\text{CuSO}_4/\text{Cu}$  compared to  $\text{KI}_3/\text{KI}$ , the parasitic reaction between  $\text{Cu}^{2+}$  and  $\text{Fe}(\text{CN})_6^{3-}$  prevents the employment of Cu-based species.<sup>15</sup>

In addition to the thermodynamic properties, the electrochemical features of redox species also play a pivotal role in regulating the output performance of the electrochemical system. Large diffusion coefficients and fast reaction kinetics are prerequisites to overcome the hindrance of mass-transport and reaction activation.<sup>16</sup> Herein rotating disk electrode (RDE) test was conducted to evaluate the two selected redox species. Fig. 2B and 2F show the respective voltammograms of  $\text{K}_3\text{Fe}(\text{CN})_6/\text{K}_4\text{Fe}(\text{CN})_6$  and  $\text{KI}_3/\text{KI}$  solutions. The limiting currents at different rotating rates indicate a mass-transport-controlled process. The diffusion coefficient,  $D$ , was calculated using the Levich equation,

$$i_{\text{lim}} = 0.62 \times nFAD^{2/3}\omega^{1/2}\nu^{-1/6}C \quad [6]$$

where  $i_{\text{lim}}$  is the limiting current controlled by diffusion,  $A$  is the electrode area,  $\omega$  is the angular rotation rate,  $\nu$  is the kinetic viscosity, and  $C$  is the concentration of redox species.<sup>17–18</sup> By curve fitting (Fig. 2C and 2G), the derived  $D$  reaches  $6.9 \times 10^{-6} \text{ cm}^2 \text{ s}^{-1}$ ,  $7.6 \times 10^{-6} \text{ cm}^2 \text{ s}^{-1}$ ,  $5.4 \times 10^{-5} \text{ cm}^2 \text{ s}^{-1}$ , and  $7.0 \times 10^{-6} \text{ cm}^2 \text{ s}^{-1}$  for  $\text{K}_4\text{Fe}(\text{CN})_6$ ,  $\text{K}_3\text{Fe}(\text{CN})_6$ ,  $\text{KI}$ , and  $\text{KI}_3$  respectively. These  $D$ -values are comparable or higher than those of typical redox species in energy storage systems.<sup>19–20</sup> Moreover, the kinetic current  $i_k$ , controlled solely by reaction kinetics without diffusion limitation, can be determined by extrapolating the rotation rate to infinity according to Koutecky–Levich equation,

$$\frac{1}{i} = \frac{1}{i_k} + \frac{1}{0.62 \times nFAD^{2/3}\omega^{1/2}\nu^{-1/6}C} \quad [7]$$

as presented in Fig. 2D and 2H. The exchange current ( $i_0$ ) is then determined by fitting the Tafel plot to the overpotential of zero (Fig. S4 ESI†), and the reaction rate constant ( $k_0$ ) can be extracted from equation shown below.

$$i_0 = nFAk_0 \quad [8]$$

The determined  $k_0$  of  $\text{K}_4\text{Fe}(\text{CN})_6/\text{K}_3\text{Fe}(\text{CN})_6$  ( $7.4 \times 10^{-4} \text{ cm s}^{-1}$ ) and  $\text{KI}/\text{KI}_3$  ( $6.7 \times 10^{-3} \text{ cm s}^{-1}$ ) can also rival those of reported redox species on carbon electrode.<sup>21–23</sup> Typically the slow mass transport will lead to a concentration gradient of redox species across the cell and thus the shift of formal potential from its equilibrium value. Moreover, an electrochemical reaction is generally controlled by the slowest reaction step, and an energy barrier must be overcome to proceed with the process, which further gives rise to the change of redox potential as voltage loss. Given the high diffusion and kinetic parameters demonstrated above, the voltage loss due to mass transport and activation polarization can be mitigated considerably by employing  $\text{K}_4\text{Fe}(\text{CN})_6/\text{K}_3\text{Fe}(\text{CN})_6$  and  $\text{KI}/\text{KI}_3$  as electroactive materials for the regenerative electrochemical cell.

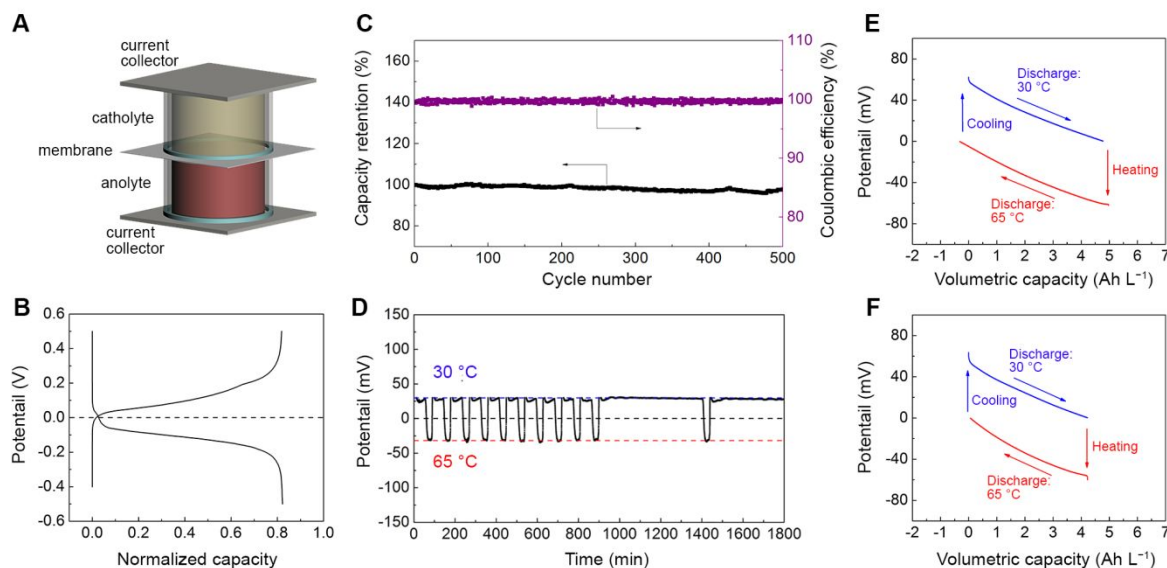
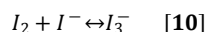


**Fig. 3** Electrochemical characteristics of the cell. (A) Schematic of the cell design. (B) The galvanostatic charge-discharge voltage profiles of the cell (0.5 M  $\text{K}_3\text{Fe}(\text{CN})_6/0.1$  M  $\text{K}_4\text{Fe}(\text{CN})_6$  versus 0.1 M  $\text{I}_2/2$  M KI) at  $6 \text{ mA cm}^{-2}$  at room temperature. (C) The corresponding cycling stability and Coulombic efficiency of the cell. (D) The open circuit voltage profile of the cell at different temperatures. (E) The galvanostatic discharge voltage profiles of the cell at  $100 \mu\text{A cm}^{-2}$ . (F) The galvanostatic discharge voltage profiles of the cell at  $200 \mu\text{A cm}^{-2}$ .

Based on the results above, a regenerative electrochemical cell was constructed with the  $\text{K}_4\text{Fe}(\text{CN})_6/\text{K}_3\text{Fe}(\text{CN})_6$  (negative  $\alpha$ ) as positive species and  $\text{KI}/\text{KI}_3$  (positive  $\alpha$ ) as negative species at room temperature. The standard electrode potential of  $\text{K}_4\text{Fe}(\text{CN})_6/\text{K}_3\text{Fe}(\text{CN})_6$  is 0.17 V lower than that of  $\text{KI}/\text{KI}_3$ , resulting in a negative output voltage of the full cell.<sup>17</sup> For the half reaction in Equation (1), the redox potential is regulated by the activity of the redox species (activity coefficient times concentration) using the Nernst equation at room temperature:

$$E = E^0 - \frac{0.059 \text{ V}}{n} \lg \frac{\gamma_B C_B}{\gamma_A C_A} \quad [9]$$

where  $E$  is the reduction potential,  $E^0$  is the standard reduction potential,  $\gamma$  is the activity coefficient, and  $C$  is the concentration.<sup>17</sup> Therefore, the potential of the full cell at room temperature can be adjusted by tuning the species ratio to maintain a positive output voltage at room temperature, in accordance with the design principle in Fig. 1. A homemade cell device, as shown in Fig. 3A and Fig. S5 (ESI<sup>†</sup>), with a membrane separator sandwiched between two quartz shells was adopted for the electrochemical test. Fig. 3B shows the typical charge-discharge voltage profiles of the cell with 0.5 M  $\text{K}_3\text{Fe}(\text{CN})_6/0.1$  M  $\text{K}_4\text{Fe}(\text{CN})_6$  as the catholyte and 0.1 M  $\text{I}_2/2$  M KI as the anolyte. Considering the high equilibrium constant ( $\sim 723$ ) of the reaction,<sup>24</sup>



0.1 M  $\text{I}_3^-$  is estimated to form when combining 0.1 M  $\text{I}_2$  and 0.1 M iodide salts. The charge and discharge curves intersect almost exactly at 0 V, which satisfies the design criteria in Fig. 1. At a high current density of  $6 \text{ mA cm}^{-2}$ , the cell can deliver a volumetric capacity of  $13.2 \text{ Ah L}^{-1}$ , indicating 82% capacity utilization of the active species. The high utilization efficiency is attributed to fast diffusion dynamics and

large reaction rate constants in view of the electrochemistry elucidated by RDE. The cycling stability of the cell is demonstrated in Fig. 3C, with capacity retention as high as 98% after 500 cycles. The capacity stability of 99.996% per cycle accompanied with the Coulombic efficiency of  $\sim 100\%$  rivals all reported energy storage systems, showing promise for the practicality of such systems.<sup>25-27</sup> The crossover of redox species depends on the selectivity of membranes and the size/charge of redox species. Thanks to the cation-exchange membrane employed here, the crossover of negatively charged species of  $\text{Fe}(\text{CN})_6^{3-}/\text{Fe}(\text{CN})_6^{4-}$  and  $\text{I}_3^-/\text{I}^-$  can be restricted greatly. The temperature-dependent operating voltage of the electrochemical system is presented in Fig. 3D, in which the cell voltage is stabilized at 30 mV at  $30^\circ\text{C}$  and  $-32 \text{ mV}$  at  $65^\circ\text{C}$ , leading to a total Seebeck coefficient up to  $-1.8 \text{ mV K}^{-1}$ . Almost no voltage variations can be observed at different temperatures over 10 cycles, exhibiting the stability of the cell system. Considering the negative Seebeck coefficient of  $\text{K}_3\text{Fe}(\text{CN})_6/\text{K}_4\text{Fe}(\text{CN})_6$  (Fig. 2A) and the positive Seebeck coefficient of  $\text{KI}_3/\text{KI}$  (Fig. 2E), the cell voltage will be larger when the temperature is lower than  $30^\circ\text{C}$  or higher than  $65^\circ\text{C}$ . In comparison, the overall potential difference is only 20 mV when  $\text{CuSO}_4/\text{Cu}$  and  $\text{Ag}/\text{AgCl}$  were employed as the cathode and the anode, respectively, indicating a total Seebeck coefficient of  $0.57 \text{ mV K}^{-1}$  (Fig. S6, ESI<sup>†</sup>). The much lower potential difference further confirms the great impact of Seebeck coefficient on the cell performance. Several systems based on the thermally regenerative electrochemical cycle were reported previously,<sup>10,28-29</sup> however, the Seebeck coefficients of the reported full cells are far from satisfactory and the solid-state electrode materials restricted the scalability of such devices. Hammond et al. reported a conceptual electrochemical cell for potential solar energy conversion, with no experimental performance demo except for the temperature dependence of open circuit voltage (due to large internal

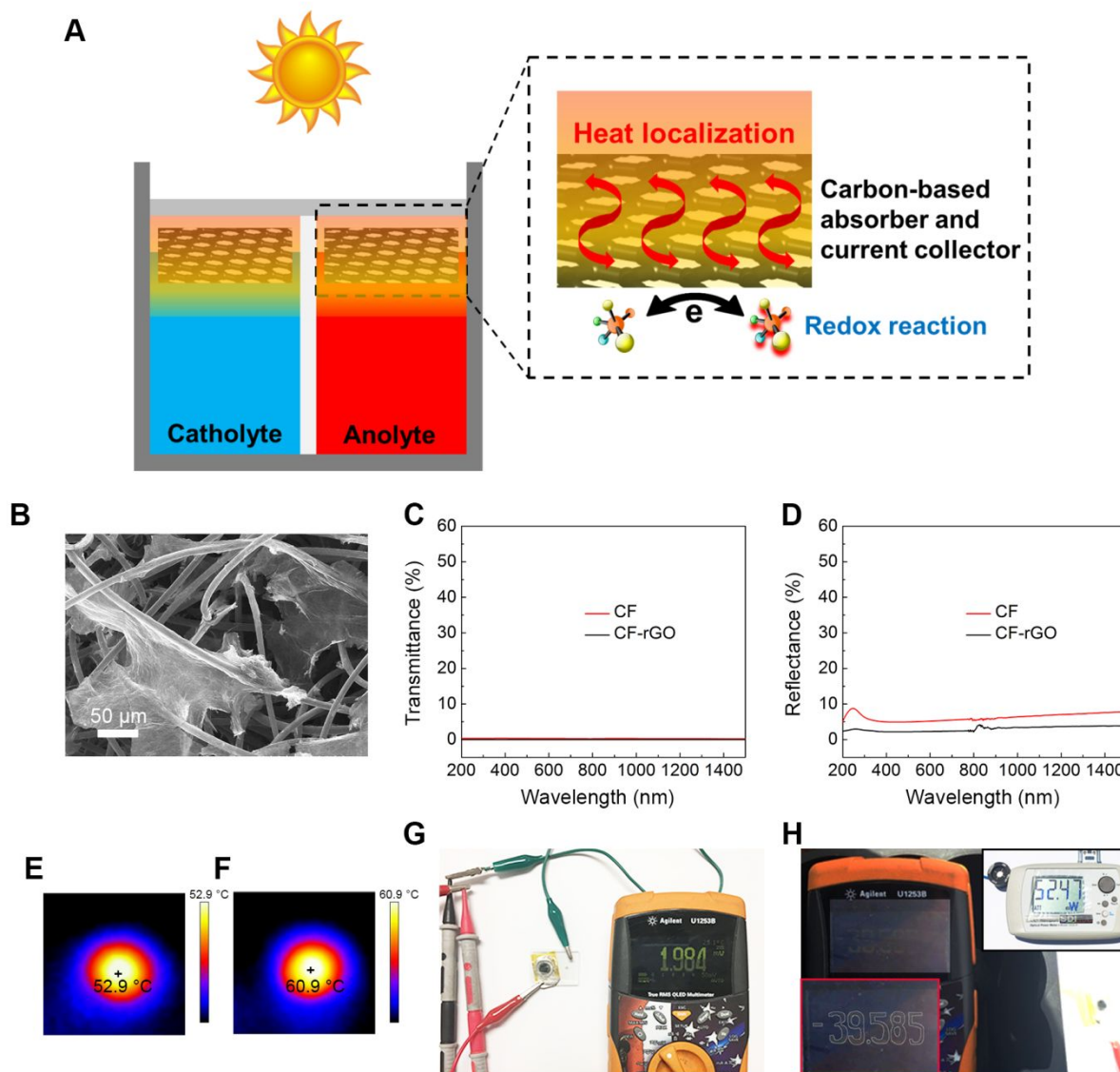


**Fig. 4** The solar-driven regenerative electrochemical cell design and characterization of absorbers. (A) Schematic of the solar-driven regenerative electrochemical cell design with the graphene-modified current collector as a solar absorber simultaneously, and the heat is localized around the current collector where the redox reaction takes place to minimize the heat loss to the bulk electrolyte solution. (B) SEM image of the graphene-modified carbon felt. (C) Transmittance spectra of different samples. (D) Reflectance spectra of different samples. (E) IR image of the carbon felt-based absorber under solar illumination of 1 sun after 30 minutes. (F) IR image of the graphene-modified absorber under solar illumination of 1 sun after 30 minutes. (G) The electrochemical cell in the discharged state at room temperature. (H) The open circuit voltage of the regenerative electrochemical cell under solar illumination on the roof of the Engineering Teaching Center building at University of Texas after 10 minutes, and the insets show the sunlight intensity measured by the optical power meter and the zoomed-in image of the display of the multimeter.

resistance and serious side reaction between reactants).<sup>30</sup> Besides, this prior system belongs to the type of nonisothermal electrochemical cells with a temperature gradient maintained between two electrodes, in sharp contrast to the isothermal cell developed in this work. Attributed to the opposite Seebeck coefficients of the positive and negative species in this work, this demonstrated  $|\alpha|$  is one of the highest compared with reported aqueous thermogalvanic cells (Table S2, ESI†). Therefore the demonstrated potential difference under such a temperature gradient is more prominent than most reported thermoelectric devices. In a typical galvanostatic discharge test (Fig. 3E and 3F), the cell was cycled

between 30 °C and 65 °C, showing round-the-clock energy delivery. It was discharged to 0 mV at 30 °C, and further heating process led to the negative voltage shift at 65 °C, thus the cell can be discharged in the opposite direction until the voltage approached 0 mV again. Finally the cell was cooled to 30 °C and the cell voltage returned to the initial value, completing the loop for extracting energy from low-grade heat sources. Fig. 3E and 3F show the voltage-capacity profiles at different current densities, and the energy conversion efficiency ( $\eta$ ) is calculated according to the equation:

$$\eta = \frac{W}{Q_H + Q_{HR}} = \frac{W_{30^\circ C} + W_{65^\circ C}}{\alpha T_H Q_c + (1 - \eta_{HR}) C_p \Delta T} \quad [11]$$

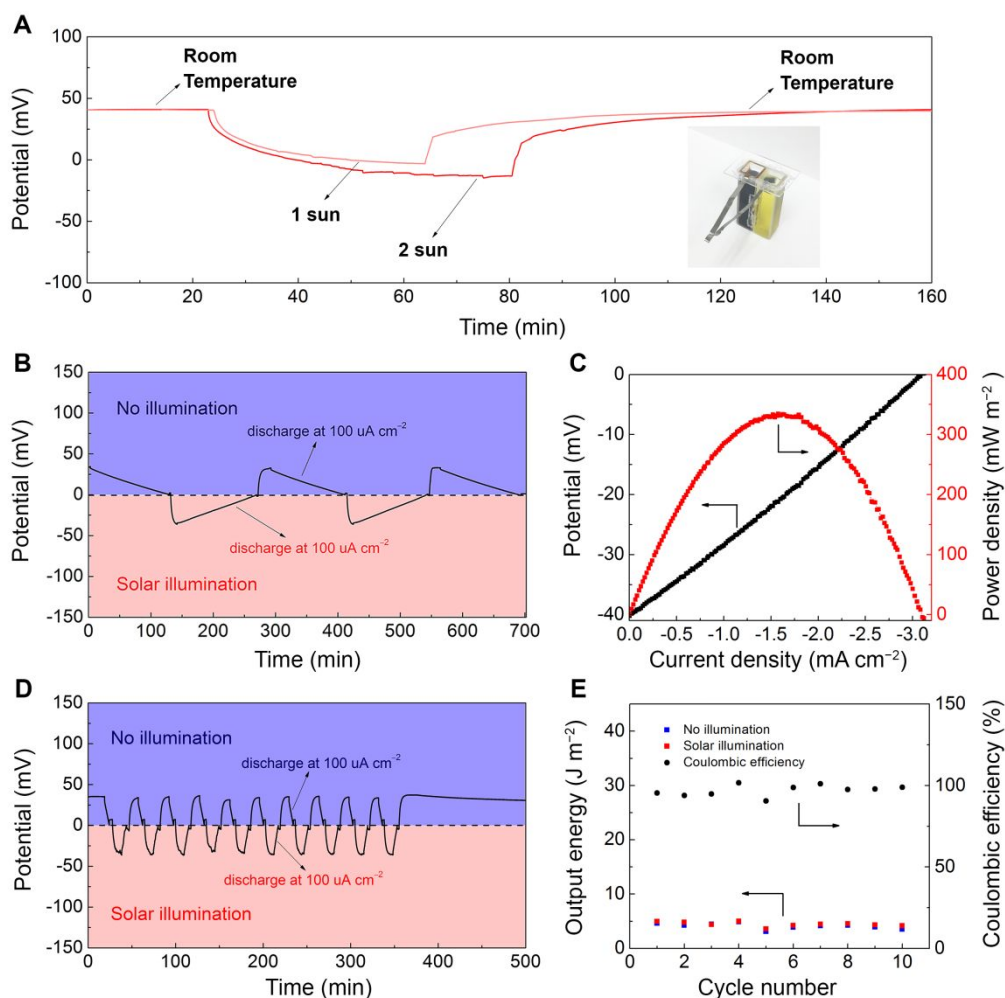
in which  $W$  is the total energy extracted from the cell at two different temperatures,  $Q_H$  is the energy absorbed at a high temperature  $T_H$ ,  $Q_{HR}$  is the energy needed to heat the whole cell device,  $Q_c$  is the cell capacity delivered at  $T_H$ ,  $\eta_{HR}$  is the heat recuperation efficiency (70% has been demonstrated as a reasonable value),  $C_p$  is the heat capacity of the cell, and  $\Delta T$  is the temperature difference.<sup>28-29</sup> The specific heat capacities of electrolytes have been tested using differential scanning calorimetry (DSC) (Fig. S7, ESI†), and the calculated efficiencies are provided in Table S3 (ESI†). The higher  $\eta$  at a lower current density is likely due to lower polarization and energy loss. Fig. S8 (ESI†) compares the energy conversion efficiencies of reported thermogalvanic cells based on redox species dissolved in solvents, which are more scalable for energy applications in contrast to solid state electrodes. It is noteworthy that the high conversion efficiency is achieved in this work thanks to the innovative cell structure and well-designed redox species, making such a novel electrochemical cell promising for efficient solar energy harvesting.

Fig. 4A illustrates the solar-driven regenerative electrochemical cell design, which is capable of converting solar energy into electrical energy based on the novel electrochemical system demonstrated above. Since the redox reactions occur at the current collector, heat localization around the current collector can minimize parasitic thermal loss to the bulk water and improve the energy conversion efficiency.<sup>31</sup> Efficient broadband solar absorption is essential for designing such an electrochemical cell.<sup>32</sup> Meanwhile, the solar absorber must also be highly conductive to facilitate electron transport during the redox reactions. Carbon felt (CF) with fibrous structures (Fig. S9, ESI†) has been widely used as low-cost, highly porous electrode backings in redox flow batteries. Graphene-based materials, with good light absorption and photothermal transduction, and high stability, are also considered promising for solar thermal applications.<sup>33</sup> In this study, we adopted a reduced graphene oxide (rGO) wrapped CF, functioning as both the solar absorber and current collector, for solar energy harvesting and storage. The rGO layers uniformly wrap the highly porous skeletons of the CF substrate, endowing it with optimized solar absorption and conductivity. Scanning electron microscope (SEM) images shown in Fig. 4B clearly reveal the tightly intertwined carbon nanofibers with graphene layers. Raman spectra of CF and rGO are shown in Fig. S10 (ESI†). The spectra display the characteristic D band around  $1350\text{ cm}^{-1}$  corresponding to disorder caused by finite crystallite size and G band around  $1580\text{ cm}^{-1}$  associated with the  $E_{2g}$  phonons at the Brillouin zone center.<sup>34</sup> The closely correlated curves of rGO and CF-rGO indicate that the surface of CF is almost entirely covered by the graphene layers. X-ray photoelectron spectroscopy (XPS) is employed to study the functional groups on carbon (Fig. S11, ESI†), and the more intensified O 1s signal of CF-rGO can lead to better hydrophilicity and thus improved reaction kinetics. The transmittance and reflectance of CF and CF-rGO were studied using a UV-vis-NIR spectrophotometer to evaluate the optical absorption ability (Fig. 4 C,D). Although both of the two samples show negligible optical transmittance in the wavelength range between 200 and 1500 nm, the reflectance of CF-rGO is remarkably reduced, suggesting better solar absorption than that of CF. It is noted that the

fluctuation can be observed between 800 nm and 900 nm in the spectrum, which is due to the change of detectors accompanied by a grating change at 800 nm of the spectrophotometer. The large optical extinction of CF-rGO is attributed to light absorption of the rGO layers wrapping the carbon nanofibers and the light scattering inside.<sup>35</sup> IR camera was used to monitor the temperature distribution on the solar absorbers under one sun. In light of the better solar absorption and photothermal activity, the temperature of CF-rGO can reach  $60.9\text{ }^\circ\text{C}$  (Fig. 4F), exceeding that of CF-based absorber ( $52.9\text{ }^\circ\text{C}$  in Fig. 4E). All these characterizations evidence CF-rGO as an excellent absorber for the solar-driven regenerative electrochemical cell.

In the open circuit voltage test with or without solar irradiation, two cuvettes containing different electrolytes were sandwiched together with a membrane separator (inset in Fig. 5A). The cuvette was drilled with a rectangular hole to enable the transport of charge carriers (Fig. S12, ESI†). Despite the outstanding photothermal capability of CF-rGO, the direct contact between the absorber and bulk water will inevitably dissipate the thermal energy considering the high thermal conductivity of water ( $\sim 0.5\text{ W K}^{-1}\text{ m}^{-1}$ ).<sup>36</sup> To better manage localized heat and restrain the parasitic heat loss, the CF-rGO solar absorber was physically separated from the bulk water by a poly(vinylidene fluoride) (PVDF)-based thermal insulator. The PVDF coating on the CF-rGO (CF-rGO-PVDF) was fabricated using a simple phase inversion method. SEM images show that the pore size is between 0.5 and  $1.5\text{ }\mu\text{m}$  (Fig. S13A, ESI†) and the thickness is  $\sim 400\text{ }\mu\text{m}$  (Fig. S13B, ESI†).<sup>37</sup> Presented in Fig. S14 (ESI†), the diameter of the circular CF-rGO absorber is 8 mm, and it is anchored in the  $10\text{ mm} \times 10\text{ mm}$  square PVDF insulator, which just fits the top section of cuvettes. The cuvette-based cell was sealed hermetically with two titanium foils extended outward as cell tabs (inset in Fig. 5A). The open circuit voltage test shows that the potential difference can reach 44 mV under one-sun illumination and improves to 55 mV under two-sun illumination (Fig. 5A). In consideration of the cell's Seebeck coefficient of  $-1.8\text{ mV K}^{-1}$ , the estimated temperature difference can reach  $\sim 24\text{ K}$  and  $\sim 31\text{ K}$  under one-sun and two-sun respectively. It is recognized that the equipment of a glass vacuum enclosure could further suppress heat loss and increase the temperature and potential difference, but would increase the system cost as well.<sup>12</sup>

In addition to monitoring the open circuit voltage under solar irradiation, galvanostatic discharge measurement was conducted on the proof-of-concept cell. An alternative cell structure demonstrated in Fig. 3A was adopted to test the cycling stability and Coulombic efficiency of the system. The cell was discharged to 1.984 mV at room temperature (Fig. 4G), and then placed on the roof of the University of Texas Engineering Teaching Center building. The sunlight intensity on the rooftop was recorded at  $52.47\text{ mW cm}^{-2}$  using an optical power meter (top-right inset in Fig. 4H). After 10 minutes, the open circuit voltage of the solar cell decreased to  $-39.585\text{ mV}$  (Fig. 4H). This amounts to a potential drop of  $\sim 41.6\text{ mV}$  contributed by both solar irradiation and temperature increase of the environment. We then simulated a comparable potential difference using artificial sunlight in the lab and extracted the battery's discharge profiles (Fig. S15, ESI†). When regarding the sunlight intensity recorded by the optical power meter as the only power source, the estimated energy conversion efficiency (the energy output divided by the irradiation time multiplied by the sunlight



**Fig. 5** The solar-driven regenerative electrochemical cell performance. (A) The open circuit voltage profile of the cell under solar illumination of 1 sun and 2 sun. (B) The galvanostatic discharge voltage profiles of the solar-driven regenerative electrochemical cell with or without solar illumination of 1 sun. (C) The polarization curve of the solar-driven regenerative electrochemical cell at a simulated open circuit voltage the same as that in Fig. 4H ( $\sim -39.6$  mV). (D) The galvanostatic discharge voltage profiles of the solar-driven regenerative electrochemical cell with or without solar illumination of 1 sun in an expedited testing process (1/8 amount of the electrolyte in Fig. 5B). (E) The cycling stability of the solar-driven regenerative electrochemical cell in Fig. 5D.

intensity) can reach 0.1% even without considering any heat recuperation efficiency. Higher energy conversion efficiencies are achievable with better heat management considering that the thermal energy conversion efficiency of 1.23% has been demonstrated above. The polarization curve at an open circuit voltage of  $-39.6$  mV was also obtained (Fig. 5C). The peak power density reaches  $332 \text{ mW m}^{-2}$ , which can be improved by optimizing the cell structure or circulating the electrolytes in flow modes to minimize the polarizations.<sup>8</sup> Fig. 5B illustrates the stability of such a solar-driven regenerative electrochemical cell, with negligible degradation detected after 700 minutes of battery cycling. Fig. 5D and 5E show the cycling stability in an expedited testing process. The cell exhibits a stabilized Coulombic efficiency of  $\sim 99\%$ , and the output energy variation may be due to temperature changes in the environment. Considering the high Coulombic efficiency, this regenerative electrochemical cell can be stored just like conventional redox flow batteries. After being fully discharged under solar illumination (Fig. 5D), the cell can just rest in the

open circuit state at room temperature and output the energy harvested whenever needed. The UV-vis spectra of both the catholyte and the anolyte before and after operation at  $65^\circ\text{C}$  are shown in Fig. S16 (ESI<sup>†</sup>), and no variations can be observed, indicating the high stability of electrolytes. Meanwhile, the SEM image and energy dispersive X-ray (EDX) elemental mapping of the current collector before and after cell operation were taken (Fig. S17, S18, ESI<sup>†</sup>), and the unaltered morphology and composition also prove the robustness of the whole system.

It is noted that this novel energy device combines advantageous features from typical energy conversion systems, such as solar cells and thermoelectric generators, and energy storage systems, such as redox flow batteries. Table S4 (ESI<sup>†</sup>) compares the bulk prices of related materials in this solar-driven regenerative electrochemical cell to those of solar cells, thermoelectrics, and redox flow batteries. Notably, compared with a representative photo-rechargeable energy system

integrating a solar cell and a redox flow battery, this solar-driven regenerative electrochemical cell is much more cost-effective considering the low cost of carbon-based solar absorbers and electroactive materials.<sup>8,38</sup> Currently the major cost in this energy device is ascribed to the Nafion-based separator, which is the widely used membrane for redox flow batteries. Therefore, developing low-cost membranes with high conductivity, selectivity, and stability will contribute to the wider implementation of both redox flow batteries and the solar-driven regenerative electrochemical cells in this work.<sup>39-40</sup>

## Conclusions

Heat is regarded as one of the most ubiquitous sources of energy in the world. Of the available solar energy reaching the earth's surface, the majority manifests itself as heat. Meanwhile, the vast majority of global energy consumption involves thermal energy in the form of heating, cooling or waste heat. Nevertheless, efficient and cost-effective thermal energy harvesting for electricity generation and storage remains a grand challenge considering the low temperature differential (<100 °C). With systematic study and rational screening of various redox species, we demonstrate a useful solar-driven regenerative electrochemical system that exploits the thermogalvanic effect for simultaneous energy harvesting and delivery. This novel energy device is based on low-cost, earth-abundant materials and can be easily assembled in scalable production processes. As a type of galvanic cell, the capacity retention of 98% can be achieved after 500 cycles with a stabilized Coulombic efficiency of ~100%.

Furthermore, we have demonstrated a high Seebeck coefficient up to  $-1.8 \text{ mV K}^{-1}$ , one of the highest values in all thermoelectric devices.<sup>13,41</sup> Even under a low temperature gradient of 35 °C, a potential differential of 62 mV can be achieved. This enables energy conversion efficiencies of 1.23% and 11.9% (versus Carnot efficiency), which are record-high for liquid thermogalvanic cells. In the proof-of-concept test under solar irradiation, the broadband and efficient solar absorption of graphene-modified absorber in conjunction with the heat localization design can lead to a reasonable temperature difference without expensive light-concentration accessories. A stable cycling performance of the solar-driven regenerative electrochemical cell has been demonstrated. The potential future applications of this cell include harvesting both the thermal energy and solar energy in remote areas, deserts for example, as a stand-alone power system. Given the much higher Seebeck coefficient demonstrated in this work than conventional thermoelectric generators, the low output voltage is mainly due to the small temperature difference.<sup>42</sup> A higher working potential can be achieved by connecting the cells in series, and a higher efficiency of energy conversion can be expected by further improving the thermal insulation and heat recuperation. The proposed solar-driven regenerative electrochemical device provides an attractive means for in situ harvesting and storage of intermittent solar energy and ubiquitous thermal energy.<sup>43</sup> It is anticipated that even better performance can be achieved by employing redox species with higher Seebeck coefficients.<sup>44</sup>

## Experimental section

**Preparation of absorbers.** GO was prepared by a modified Hummers' method,<sup>45</sup> and the CF-rGO was fabricated in a dip coating and reduction process. The CF was first treated with ozone to improve the hydrophilicity, and then it was immersed in the GO solution (8.1 mg mL<sup>-1</sup>) until it is fully wetted. Hydrazine hydrate solution was added into the GO solution containing CF, and the mixture was heated at 80 °C for 10 hours under reflux to fully reduce GO. The obtained CF-rGO was rinsed with water and finally dried in a vacuum oven at 90 °C overnight. To coat the CF-rGO with a 400 μm thick PVDF layer, a typical phase inversion method was adopted. The PVDF powder was mixed with NMP under the mass ratio of 18%, and the mixture was kept at 60 °C under stirring for 24 h, followed by degassing in vacuum oven overnight to make a dilute solution without bubbles. The PVDF solution was cast on a glass plate with Kapton tapes to control the thickness. Then the CF-rGO was put on top of the PVDF solution, and the glass plate was immediately immersed in water to achieve phase inversion. Because the thickness of CF-rGO is higher than the depth of the PVDF solution, only one side of CF-rGO in contact with the solution will be coated with PVDF. The prepared CF-rGO-PVDF absorber was immersed in water for two days, and the water was changed twice to make sure the residual solvent inside will be removed. Finally the absorber was rinsed with ethanol and dried at room temperature for use. The CF-rGO-PVDF absorber will be immersed in the electrolyte when the cell is working.

**Device assembly.** The cell components for the device in Fig. 3A are shown in Fig. S5A(ESI†). First, a Nafion membrane was sandwiched between two cylindrical quartz shells (inner diameter: 8 mm) by heating Surllyn resin sealant at 120 °C for 5 hours. Second, a mixture of Super P carbon black with PVDF (mass ratio of 9:1) was dispersed in NMP solvent to form a slurry, and the Ti foil was coated with the slurry using a doctor blade to make the current collector. The Ti foil was drilled with a hole in advance for the injection of electrolytes. Third, the Ti-based current collectors were adhered to the quartz shells using Surllyn resin sealant as well. Photographs of the assembled cell device are shown in Fig. S5, B and C(ESI†). The solar-driven regenerative electrochemical cell was built similarly except for using the ITO-based current collector and inserting the CF-rGO inside the quartz shell to absorb solar irradiation. The cuvette-based device was also assembled to test the open circuit voltage, and the Nafion was sandwiched between two cuvettes with predrilled holes (Fig. S11, ESI†) sealed with Surllyn resin sealant as well.

**Characterizations.** All the electrochemical characterizations were conducted on a BioLogic VMP3 potentiostat system. The Seebeck coefficient of most redox species was tested using a three-electrode setup with the Ag/AgCl/4M KCl as reference electrode, platinum wire as the counter electrode, and glassy carbon as the working electrode. For the Seebeck coefficient test of CuSO<sub>4</sub>/Cu solution, the working electrode is a Cu foil instead of the glassy carbon. The open circuit voltage was monitored at different temperatures controlled by water bath.

The RDE measurements were conducted on the BioLogic RRDE-3A rotating ring disk electrode using the Ag/AgCl/4M KCl as reference electrode, platinum wire as the counter electrode, and glassy carbon as the working electrode. The Raman spectra were tested on a Micro-

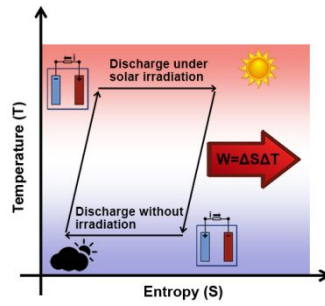
Raman Spectrometer (Witec, Alpha 300) under 488 nm. SEM (scanning electron microscope) images were taken on Hitachi S-5500. DSC test was conducted on the TGA/DSC 1 thermogravimetric analyzer by Mettler Toledo. The transmittance and reflectance of CF and CF-rGO were studied using a UV-vis-NIR spectrophotometer (Cary 5000) with an integrating sphere unit. The UV-vis spectra of samples were recorded using a UV-vis spectrometer (Evolution 300, Thermo Scientific). The thermal images were taken by an infrared camera (Fluke). The solar simulator (AbetTech, M-LS Rev B) was adopted for the cell test. The solar flux was calibrated with a thermopile (Newport, 818SL) connected to a power meter (Newport, 1916-R).

## Acknowledgements

G.Y. acknowledges the financial support from the National Science Foundation award (NSF-CMMI-1537894), Alfred P. Sloan Research Fellowship, and Camille Dreyfus Teacher-Scholar Award.

## References

- D. J. Lipomi and Z. Bao, *Energy Environ. Sci.*, 2011, **4**, 3314-3328.
- J. Zhu, Z. Yu, S. Fan and Y. Cui, *Mater. Sci. Eng. R Rep.*, 2010, **70**, 330-340.
- M. Yu, X. Ren, L. Ma and Y. Wu, *Nat. Commun.*, 2014, **5**, 5111.
- Y. Liu, N. Li, S. Wu, K. Liao, K. Zhu, J. Yi and H. Zhou, *Energy Environ. Sci.*, 2015, **8**, 2664-2667.
- N. Li, Y. Wang, D. Tang and H. Zhou, *Angew. Chem. Int. Ed.*, 2015, **54**, 9271-9274.
- L. A. Weinstein, J. Loomis, B. Bhatia, D. M. Bierman, E. N. Wang and G. Chen, *Chem. Rev.*, 2015, **115**, 12797-12838.
- Y. Zhou, T. Kurosawa, W. Ma, Y. Guo, L. Fang, K. Vandewal, Y. Diaoyang, C. Wang, Q. Yan, J. Reinspach, J. Mei, A. L. Appleton, G. I. Koleilat, Y. Gao, S. C. B. Mannsfeld, A. Salleo, H. Ade, D. Zhao and Z. Bao, *Adv. Mater.*, 2014, **26**, 3767-3772.
- Q. Cheng, W. Fan, Y. He, P. Ma, S. Vanka, S. Fan, Z. Mi and D. Wang, *Adv. Mater.*, 2017, **29**, 1700312.
- T. I. Quickenden and Y. Mua, *J. Electrochem. Soc.*, 1995, **142**, 3985-3994.
- S. W. Lee, Y. Yang, H.-W. Lee, H. Ghasemi, D. Kraemer, G. Chen and Y. Cui, *Nat. Commun.*, 2014, **5**, 3942.
- C. Gao, S. W. Lee and Y. Yang, *ACS Energy Lett.*, 2017, **2**, 2326-2334.
- D. Kraemer, Q. Jie, K. McEnaney, F. Cao, W. Liu, L. A. Weinstein, J. Loomis, Z. Ren and G. Chen, *Nat. Energy*, 2016, **1**, 16153.
- A. Gunawan, C.-H. Lin, D. A. Buttry, V. Mujica, R. A. Taylor, R. S. Prasher and P. E. Phelan, *Nanoscale Microsc Therm.*, 2013, **17**, 304-323.
- Y. Ding, Y. Zhao, Y. Li, J. B. Goodenough and G. Yu, *Energy Environ. Sci.*, 2017, **10**, 491-497.
- C. D. Wessells, R. A. Huggins and Y. Cui, *Nat. Commun.*, 2011, **2**, 550.
- Y. Ding, Y. Zhao and G. Yu, *Nano Lett.*, 2015, **15**, 4108-4113.
- A. J. Bard and L. R. Faulkner, *Electrochemical Methods: Fundamentals and Applications*, 2nd ed., 2001, **Wiley, Hoboken**.
- Y. Ding and G. Yu, *Angew. Chem. Int. Ed.*, 2016, **55**, 4772-4776.
- Q. Zheng, Z. Niu, J. Ye, S. Zhang, L. Zhang, L. Li, Y. Zhao and X. Zhang, *Adv. Funct. Mater.*, 2017, **27**, 1604299.
- X. Wei, L. Cosimbescu, W. Xu, J. Z. Hu, M. Vijayakumar, J. Feng, M. Y. Hu, X. Deng, J. Xiao, J. Liu, V. Sprenkle and W. Wang, *Adv. Energy Mater.*, 2015, **5**, 1400678.
- M. Park, J. Ryu, W. Wang and J. Cho, *Nat Rev Mater*, 2016, **2**, 16080.
- C. Wang, Q. Lai, P. Xu, D. Zheng, X. Li and H. Zhang, *Adv. Mater.*, 2017, **29**, 1605815.
- Y. Ding, C. Zhang, L. Zhang, Y. Zhou and G. Yu, *Chem. Soc. Rev.*, 2018, **47**, 69-103.
- Y. Zhao, L. Wang and H. R. Byon, *Nat. Commun.*, 2013, **4**, 1896.
- Y. Yang, G. Zheng and Y. Cui, *Energy Environ. Sci.*, 2013, **6**, 1552-1558.
- Y. Wang, P. He and H. Zhou, *Adv. Energy Mater.*, 2012, **2**, 770-779.
- J. Liu, J. G. Zhang, Z. Yang, J. P. Lemmon, C. Imhoff, G. L. Graff, L. Li, J. Hu, C. Wang, J. Xiao, G. Xia, V. V. Viswanathan, S. Baskaran, V. Sprenkle, X. Li, Y. Shao and B. Schwenzer, *Adv. Funct. Mater.*, 2013, **23**, 929-946.
- Y. Yang, J. Loomis, H. Ghasemi, S. W. Lee, Y. J. Wang, Y. Cui and G. Chen, *Nano Lett.*, 2014, **14**, 6578-6583.
- Y. Yang, S. W. Lee, H. Ghasemi, J. Loomis, X. Li, D. Kraemer, G. Zheng, Y. Cui and G. Chen, *Proc. Natl. Acad. Sci. U.S.A.*, 2014, **111**, 17011-17016.
- R. H. Hammond and W. M. Risen, *Solar Energy*, 1979, **23**, 443-449.
- H. Ghasemi, G. Ni, A. M. Marconnet, J. Loomis, S. Yerci, N. Miljkovic and G. Chen, *Nat. Commun.*, 2014, **5**, 4449.
- L. Zhou, Y. Tan, J. Wang, W. Xu, Y. Yuan, W. Cai, S. Zhu and J. Zhu, *Nat. Photonics*, 2016, **10**, 393.
- P. Zhang, J. Li, L. Lv, Y. Zhao and L. Qu, *ACS Nano*, 2017, **11**, 5087-5093.
- H. Ren, M. Tang, B. Guan, K. Wang, J. Yang, F. Wang, M. Wang, J. Shan, Z. Chen, D. Wei, H. Peng and Z. Liu, *Adv. Mater.*, 2017, **29**, 1702590.
- Y. Li, T. Gao, Z. Yang, C. Chen, W. Luo, J. Song, E. Hitz, C. Jia, Y. Zhou, B. Liu, B. Yang and L. Hu, *Adv. Mater.*, 2017, **29**, 1700981.
- X. Li, W. Xu, M. Tang, L. Zhou, B. Zhu, S. Zhu and J. Zhu, *Proc. Natl. Acad. Sci. U.S.A.*, 2016, **113**, 13953-13958.
- C. Dong, G. He, H. Li, R. Zhao, Y. Han and Y. Deng, *J. Membrane Sci.*, 2012, **387-388**, 40-47.
- N. F. Yan, G. R. Li and X. P. Gao, *J. Mater. Chem. A*, 2013, **1**, 7012-7015.
- W. Lu, Z. Yuan, Y. Zhao, H. Zhang, H. Zhang and X. Li, *Chem. Soc. Rev.*, 2017, **46**, 2199-2236.
- X. Yan, C. Zhang, Y. Dai, W. Zheng, X. Ruan and G. He, *J. Membrane Sci.*, 2017, **544**, 98-107.
- W. Liu, X. Yan, G. Chen and Z. Ren, *Nano Energy*, 2012, **1**, 42-56.
- M. Zebajradi, K. Esfarjani, M. S. Dresselhaus, Z. F. Ren and G. Chen, *Energy Environ. Sci.*, 2012, **5**, 5147-5162.
- D. Li, G. S. Wu, W. Wang, Y. D. Wang, D. Liu, D. C. Zhang, Y. F. Chen, G. P. Peterson and R. Yang, *Nano Lett.*, 2012, **12**, 3385-3390.
- H. Zhou and P. Liu, *ACS Applied Energy Materials*, 2018, **1**, 1424-1428.
- D. C. Marciano, D. V. Kosynkin, J. M. Berlin, A. Sinititskii, Z. Sun, A. Slesarev, L. B. Alemany, W. Lu and J. M. Tour, *ACS Nano*, 2010, **4**, 4806-4814.



An innovative energy system integrating energy conversion and storage is designed to achieve cost-effective harnessing of solar energy and thermal energy.